



1 HailCam: An Automated Imaging System for Real-Time 2 Measurement of Hail Size Distributions and Fall Rates

3 Baolei Lyu^{1,2}, Hui Wang³, Tianlei Gao^{1,2}, Zhanfu Yin³, Xiaofeng Lou³, Yugang Duan^{1,2}, Yihang Huang^{1,2},
4 Zhiqiang Zhao³

5 ¹ Huayun Sounding Meteorological Technology Co. Ltd, Beijing, 102200, China

6 ² Key Laboratory of Intelligent Meteorological Observation Technology, Beijing 100081, China

7 ³ CMA Key Laboratory of Cloud-Precipitation Physics and Weather Modification (CPML), CMA Weather Modification Centre
8 (WMC), Beijing 100081, China

9 *Correspondence to:* Baolei Lyu (baoleilv@foxmail.com), Hui Wang (hwang@cma.gov.cn), Zhanfu Yin (yin_zf@126.com)

10 **Abstract.** Ground-based hail observations with high temporal resolution and precise microphysical quantification remain
11 critically scarce, limiting the validation of radar-based hail detection algorithms and convective-scale numerical models.
12 Existing automatic hail sensors often suffer from small sampling areas, susceptibility to rain interference, and limited
13 automation in post-event processing. We present HailCam, an intelligent hail observation instrument integrating high-
14 definition optical imaging, automated particle collection, and real-time deep learning inference to address critical gaps in time-
15 resolved ground-based hail microphysics measurements. The system employs a ConvNeXt-Tiny architecture with Mask R-
16 CNN for instance segmentation, capturing hailstone number, size distribution, and number flux at one-minute intervals over a
17 60 cm × 60 cm sampling area. Laboratory validation using synthetic ice spheres (5–45 mm) and polystyrene foam spheres
18 demonstrates 91% sizing accuracy within ±5% relative error (RMSE 0.21–1.71 mm) and counting linearity of $R^2 = 0.9989$.
19 Field intercomparison with an OTT Parsivel² disdrometer during a nocturnal hail event on 9 May 2025 reveals consistent
20 temporal evolution of hailfall and statistically indistinguishable size distributions (Kolmogorov-Smirnov $D = 0.167$ – 0.250 , $p >$
21 0.84), though absolute counts differ due to distinct phase-discrimination methodologies. HailCam provides co-located, time-
22 stamped measurements essential for validating radar-based hail algorithms and constraining convective-scale numerical
23 models, particularly in complex terrain where remote sensing is challenged.

24 1 Introduction

25 Hail is a highly localized yet destructive form of solid precipitation generated within intense convective storms (Allen et al.,
26 2020). Its formation involves complex microphysical processes, wherein supercooled water droplets are lofted by strong
27 updrafts, freeze, and undergo repeated cycles of accretion to form hailstones that eventually fall to the surface (Pflaum, 1984;
28 Knight and Charles, 2010). Due to its sporadic occurrence, typically less than once per year at any given location in Europe
29 (Punge and Kunz, 2016), and only two to three events per square kilometer annually even in hail-prone regions such as
30 Switzerland (Nisi et al., 2018), hail poses significant challenges for systematic observation and climatological analysis.
31 Accurate, high-resolution observational data on hail properties, including particle size distribution, number concentration, mass
32 flux, and temporal evolution, are essential not only for understanding hail microphysics and storm dynamics but also for
33 validating numerical weather prediction models (Wobrock et al., 2003), improving radar-based hail detection algorithms, and
34 supporting risk assessment in agriculture, infrastructure, and insurance sectors (Allen et al., 2020; Martius et al., 2018).
35 Two principal approaches are employed to observe hail, which are remote sensing and surface (ground-truth) measurements.
36 Remote sensing techniques, primarily using weather radar, e.g., dual-polarization Doppler systems (Smyth et al., 1999; Pilorz
37 et al., 2022), or meteorological satellites (Ravinder et al., 2013; Mroz et al., 2017), provide spatially extensive coverage and



38 early warning capabilities. However, these methods rely on indirect proxies, such as reflectivity, differential reflectivity, or
39 cloud-top temperature, to infer hail presence and intensity. Consequently, they suffer from inherent ambiguities and require
40 validation against direct ground observations, especially in complex terrain where beam blockage or attenuation can degrade
41 data quality (Skripnikova and Rezacova, 2014).

42 In contrast, surface-based observations offer direct, physically grounded measurements. These include manual reports from
43 observer networks, crowdsourced data via mobile applications (Barras et al., 2019), insurance loss records (Fonseca-Cerda et
44 al., 2026), storm chaser documentation (List et al., 2010a), drone surveys (Soderholm et al., 2020), and instrumented networks
45 such as hailpads (Nisi et al., 2018). Among these, hailpad networks have been historically dominant due to their low cost and
46 simplicity (Dessens et al., 2007; Sánchez et al., 2009; Changnon, 1970). Hailpads, typically made of extruded polystyrene
47 foam, record impact craters that are later analyzed to estimate hailstone diameter under assumptions of spherical shape and
48 constant density (Cheng and English, 1983; List et al., 2010b). Despite their widespread use, hailpads provide only time-
49 integrated, post-event data with no information on the precise timing, sequence, or evolution of individual hail impacts, a
50 critical limitation for studying hailfall dynamics.

51 To address this gap, time-resolving automatic hail sensors have emerged as a promising solution. Early prototypes, such as the
52 hail spectrometer used by Federer and Waldvogel (1975), captured sequential images of hailstones before removal. More recent
53 instruments include impact disdrometers (Li et al., 2024) and piezoelectric sensors that record impact timing and kinetic energy
54 (Löffler-Mang et al., 2011; Bhandari et al., 2025). Notably, Switzerland completed in 2020 the deployment of a national
55 network of 80 automatic hail sensors capable of timestamping individual impacts and estimating hailstone size and energy
56 (Kopp et al., 2023a; Kopp et al., 2023b). Yet, such systems remain scarce globally, and comprehensive datasets with
57 simultaneous measurements of hail size, count, and temporal structure are still exceptionally rare. Moreover, existing automatic
58 sensors often face limitations, such as small sampling areas reducing statistical representativeness, susceptibility to rain
59 interference with false positives. As climate change is projected to increase hail frequency and severity in many regions
60 (Raupach et al., 2021; Dessens et al., 2015), the demand for robust, multi-parameter, real-time hail observation systems has
61 been great.

62 In response to these challenges, we present an intelligent, deep learning–embedded hail observation instrument that integrates
63 high-definition imaging, automated hail collection in a large sampling area with fixed time interval. By leveraging the
64 ConvNeXt architecture for object detection, our system captures hailstone number, size distribution, and thus number flux,
65 providing unprecedented granularity in ground-based hail characterization. This paper details the instrument design,
66 algorithmic framework, laboratory validation, and error analysis—laying the foundation for scalable, high-fidelity hail
67 monitoring networks. The general structure and observation principles of the instrument are described in Section 2.1, with
68 practical realizations and workflows of the algorithms are detailed in Section 2.2. Evaluations of observation data by the
69 instrument and related error analysis are demonstrated in Section 4.

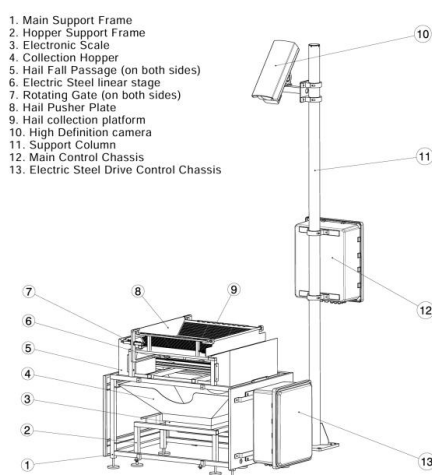
70 **2 Hail Intelligent Observation Algorithm and Device**

71 **2.1 Instrument Architecture and Physical Modelling Framework**

72 The intelligent hail observation system presented in this study is designed to address three core observational gaps in current
73 image-based hail monitoring: the lack of time-resolved hailstone counts, unfixed observation area, and limited automation in
74 post-event data processing. To achieve these objectives, the instrument integrates mechanical collection, optical imaging, and
75 real-time deep learning inference within a unified, weatherproof enclosure. As illustrated in Figure 1, the instrument comprises
76 four functional modules. First, the instrument has a relatively large square collection aperture with side length = 60 cm fitted
77 with a bar grid having 0.4 cm spacing (component 9). This grid acts as a mechanical filter: it is designed to allow rainwater



78 and small hydrometeors (such as typical graupel and small ice pellets) to drain through, while retaining larger hail particles
 79 (≥ 5 mm) on the grid surface for imaging.. Second, it contains an automated swiping mechanism (component 8) that conveys
 80 collected particles from the funnel base to a standardized imaging platform every minute during active precipitation . Third, a
 81 high-resolution imaging subsystem (component 10), consisting of a 8-megapixel RGB camera (pixel size = 1.55 μm) equipped
 82 with automatic low-light compensation paired with integrated diffuse LED illumination to eliminate specular reflections and
 83 ensure consistent contrast for particle segmentation even in nocturnal conditions. Lastly, HailCAM is deployed with
 84 an NVIDIA Jetson Nano embedded computing platform, which delivers a peak AI inference performance of approximately 0.5
 85 TOPS (trillion operations per second) under INT8 precision.



86
87

88 **Figure 1: The major components of the hail observation device (left panel). Note: An electronic scale is installed beneath the**
 89 **collection tray for experimental mass validation (not used in the current automated algorithm). Photo of the HailCam deployed at**
 90 **the Weining Hail Suppression Experimental Base.**

91 Unlike traditional disdrometers that infer particle size from impact momentum or acoustic signatures, our approach relies on
 92 direct geometric measurement. Each hailstone is treated as an oblate spheroid, and its projected equivalent hailstone diameter
 93 and fall rates are extracted from the binary image via deep learning segmentation.
 94 The system operates by consecutively capturing high-resolution image on a fixed duty cycle up to 20 seconds with a default
 95 60-second configuration, ensuring compatibility with standard meteorological reporting intervals. Specifically, it takes one
 96 single image at the 00-second mark of every sampling interval, which is 00 second in the experimental instrument in Weining.
 97 This enables continuous, unattended operation over multi-day storm sequences, a critical capability for capturing the full
 98 lifecycle of prolonged hail events. Once hailstones are detected by in the image processing module, HailCam evacuates tray
 99 to clean up the sampling area. In general, the instrument’s architecture bridges the gap between passive collectors (e.g., hailpads)
 100 and high-frequency but low-fidelity impact sensors by delivering co-located, time-stamped measurements of hailstone count,
 101 and size distribution. All features are derived from physically interpretable observables rather than indirect proxies

102 2.2 Deep Learning–Based Hailstone Segmentation and Characterization

103 Accurate identification and quantification of individual hailstones from raw imagery constitute a critical step in deriving
 104 physically meaningful microphysical parameters. Traditional computer vision approaches, such as thresholding, edge detection,
 105 or watershed segmentation, are highly sensitive to variations in lighting, surface wetness, and particle overlap, leading to

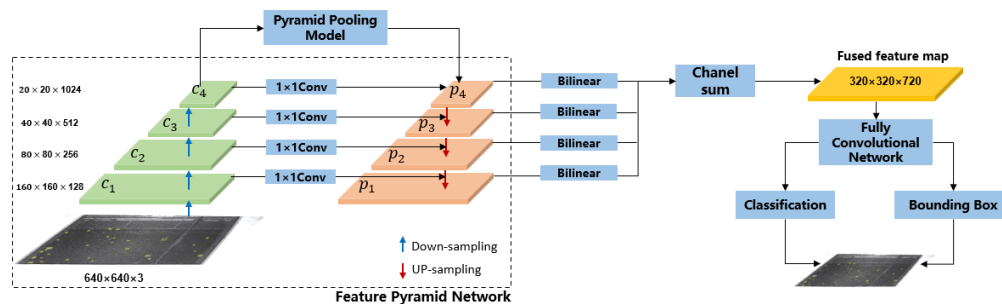


106 substantial under- or over-counting in real-world conditions. To overcome these limitations, we implement an end-to-end deep
107 learning pipeline based on the ConvNeXt architecture (Liu et al., 2022), which has demonstrated state-of-the-art performance
108 in dense object detection tasks while maintaining computational efficiency suitable for edge deployment.

109 2.2.1 Network Architecture and Training Protocol

110 The core of our algorithm is a modified ConvNeXt-Tiny backbone integrated with a Feature Pyramid Network (FPN) head for
111 multi-scale feature fusion, followed by a Mask R-CNN-style instance segmentation head. This architecture implements a
112 hierarchical feature learning strategy to address the challenges of dense hail detection. First, the ConvNeXt-Tiny backbone
113 employs a modern ConvNet design with large convolutional kernels and a LayerNorm-centric architecture. It processes the
114 input image through multiple stages, progressively extracting semantic features while reducing spatial resolution. This provides
115 a robust foundation for visual representation learning. Second, the Feature Pyramid Network (FPN) is applied to the outputs
116 of the ConvNeXt backbone. The FPN constructs a pyramid of feature maps by top-down lateral connections. This mechanism
117 allows the fusion of strong semantic information from deeper layers with high-resolution spatial details from shallower layers.
118 Consequently, the model achieves scale invariance, enabling accurate detection of hailstones ranging from small fragments to
119 large aggregates. Finally, the Mask R-CNN-style head operates on this fused feature pyramid to perform instance segmentation.
120 It utilizes a Region Proposal Network (RPN) to generate candidate object bounding boxes. For each candidate region, the
121 network branches into three parallel outputs: (1) a classifier to confirm the presence of hail, (2) a regressor to refine the
122 bounding box coordinates, and (3) a Fully Convolutional Network (FCN) mask branch that predicts a binary segmentation
123 mask for the hailstone at pixel resolution. This allows the system to distinguish individual hailstones even in scenarios of slight
124 overlap, providing precise geometric boundaries for diameter calculation.

125 This configuration enables simultaneous prediction of bounding boxes, semantic masks, and confidence scores for each
126 detected hailstone. The input to the network is a 640×640-pixel RGB image captured under controlled diffuse illumination.



127

128 **Figure 2: work flow of model detection algorithm.**

129 Training data were generated from a curated dataset of 8,742 manually annotated images collected during the hail season in
130 2024, encompassing diverse hail morphologies (spherical, conical, irregular), sizes (5–45 mm equivalent diameter), and
131 surface conditions (dry, wet, partially melted). To enhance robustness, we applied photometric augmentations (e.g., random
132 brightness/contrast shifts) and geometric transformations (rotation, scaling, elastic deformation) during training. The model
133 was optimized using the AdamW optimizer with a cosine-annealed learning rate (initial = 3×10^{-4}) and a composite loss function
134 combining focal loss for classification, smooth L1 loss for box regression, and Dice loss for mask refinement. Crucially, the
135 deep learning approach eliminates the need for manual tuning of segmentation thresholds, adapts dynamically to changing
136 environmental conditions, and achieves a high particle detection accuracy.

137 2.2.2 Model Inference and Post-Processing

138 During operational inference, the trained model processes each one-minute image frame in real time on an embedded GPU



139 (NVIDIA Jetson Nano). Detected instances with a confidence score below 0.7 are discarded to suppress false positives from
140 water droplets, debris, or imaging artifacts. Overlapping detections ($\text{IoU} > 0.5$) are resolved via non-maximum suppression
141 (NMS), ensuring one-to-one correspondence between physical particles and predicted masks.

142 To recover the physical dimensions of each segmented retained instance within the imaged hail collection tray, we formulate
143 the problem as a metric reconstruction from a single calibrated perspective view. The tray contains a known square reference
144 pattern of side length L , lying on the plane $Z=0$ of the world coordinate system. Given the camera's intrinsic matrix \mathbf{K} and
145 extrinsic parameters (\mathbf{R}, \mathbf{t}) —obtained via prior calibration—we compute the homography \mathbf{H} that maps points on this plane to
146 image pixels:

$$147 \quad \mathbf{H} = \mathbf{K}[\mathbf{r}_1 \mathbf{r}_2 \mathbf{t}] \quad (1)$$

148 where $\mathbf{r}_1, \mathbf{r}_2$ are the first two columns of the rotation matrix \mathbf{R} . The four corners of the region of interest are detected in the
149 image as $\mathbf{p}_i = (u_i, v_i)^t (i = 1, \dots, 4)$. After correcting for lens distortion, these points are back-projected onto the $Z=0$ plane
150 using \mathbf{H}^{-1} , yielding their metric coordinates (X_i, Y_i) . The real-world width and height are then obtained via Euclidean distances
151 between corresponding corner pairs. This approach enables pixel-to-millimeter conversion with sub-millimeter accuracy. In
152 cases where extrinsic parameters are unknown, they can be estimated by solving a Perspective-n-Point (PnP) problem using
153 the detected corners of the full reference square, as detailed in the Text S1 in the Supplementary Material.

154 For each retained instance, hailstone diameter could be obtained under the assumption that hailstone is a standard sphere. The
155 equivalent diameter D_i in physical units (mm) is then derived as:

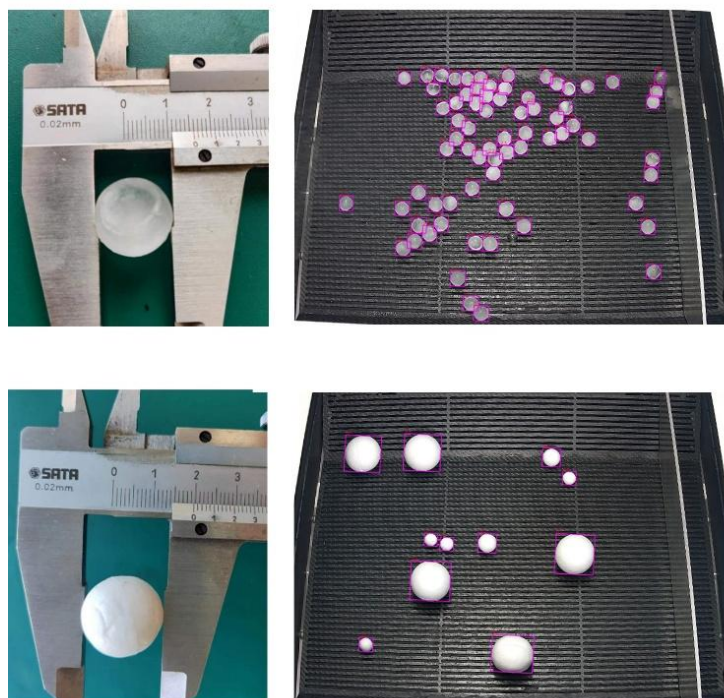
$$156 \quad D_i = \frac{|X_{i, \text{left}} - X_{i, \text{right}}| + |Y_{i, \text{top}} - Y_{i, \text{bottom}}|}{2} \quad (2)$$

157 While this assumes spheric shape, a simplification that introduces bias for highly elongated or fragmented stones, it aligns
158 with standard practice in optical disdrometry and provides consistency with radar-based size definitions, e.g., maximum
159 dimension in dual-polarization retrievals (Skripnikova and Rezacova, 2014).

160 **2.3 Experimental Validation and Uncertainty Quantification**

161 To establish the metrological credibility of the intelligent hail observation system, we conducted a multi-stage validation
162 protocol encompassing controlled laboratory experiments, and side-by-side field intercomparisons. This section details the
163 experimental design for key observables: hailstone count, and equivalent diameter.

164 **2.3.1 Laboratory Calibration with Artificial Hailstones**



165

166 **Figure 3: Balls of the same material and size placed in batches with different quantities on the equipment to calculate the average**
167 **diameter.**

168 Due to the inherent unpredictability of natural hail events in terms of timing, location, and intensity, laboratory-based validation
169 experiments were conducted to quantitatively assess the measurement accuracy of the HailCam system. Two complementary
170 experimental protocols were designed to independently evaluate the instrument's sizing and counting capabilities.

171 Synthetic hailstones were fabricated using distilled water frozen in spherical molds under controlled laboratory conditions.
172 Seven nominal diameter classes were produced: 5, 7.5, 10, 15, 20, 35, and 45 mm, encompassing the typical size range
173 observed in mid-latitude severe storms (Nisi et al., 2018). For each size class, 50 ice spheres were randomly dropped onto the
174 collection tray. The automated imaging pipeline subsequently captured and processed the projected silhouettes of these
175 particles. The instrument-derived equivalent diameters were compared against the reference diameters measured using a
176 precision digital caliper (± 0.01 mm accuracy) to quantify sizing accuracy and precision across the operational range.

177 To assess the system's quantification accuracy under varying particle number densities, expanded polystyrene foam spheres of
178 mixed diameters (ranging from 5 to 30 mm) were employed as proxy hailstones. A total of 96 independent trials were conducted,
179 with each trial involving the manual placement of 3 to 250 foam spheres on the collection tray in randomized spatial
180 configurations. This range was selected to evaluate performance from sparse distributions (representative of marginal hailfall
181 conditions) to dense accumulations (approaching the upper limit of typical hailstorm intensities). The automated detection
182 algorithm processed each image frame, and the retrieved particle counts were compared against the ground-truth counts
183 established through manual enumeration.

184 The ice sphere experiments specifically targeted sizing fidelity under controlled morphological conditions, while the foam
185 sphere trials focused on counting accuracy across a broad dynamic range of particle concentrations. The combination of these
186 two protocols enables comprehensive characterization of both the metrological traceability of individual particle measurements



187 and the statistical robustness of population estimates derived from the imaging system.

188 **2.3.2 Field Intercomparison with Reference Instruments**

189 To evaluate the performance of the HailCam system under complex natural climatic, topographic and illumination conditions,
190 co-located field intercomparisons were conducted at the Weining Hail Suppression Experimental Base of the China
191 Meteorological Administration (CMA), located in Guizhou Province (26.9°N, 104.9°E), as shown in Figure 1. This study area
192 is characterized by typical karst terrain with rugged relief and frequent severe convective weather, posing rigorous practical
193 tests for the stability, anti-interference and detection accuracy of hail observation instruments in complex underlying surface
194 environments.

195 A co-located OTT Parsivel² laser disdrometer (hereinafter referred to as disdrometer) was deployed alongside the HailCam
196 system as the reference instrument. The disdrometer is a widely utilized optical precipitation spectrometer that measures
197 particle size distributions and fall velocities based on the extinction of a horizontal laser beam by hydrometeors passing through
198 the sampling area (Löffler-Mang and Joss, 2000). The OTT Parsivel² has a nominal size accuracy of ± 1 bin (approximately \pm
199 0.125 mm for small particles, scaling non-linearly) under laboratory conditions, though field accuracy can be affected by
200 turbulence and alignment (Tokay et al., 2014). The device provides size distributions across 32 diameter classes ranging from
201 0.062 to 24.5 mm, and has been widely used reference instrument for hydrometeor particle size and fall velocity measurement
202 (Tokay et al., 2014; Löffler-Mang and Joss, 2000). The disdrometer was set to its standard operational mode with a 1-minute
203 sampling interval, consistent with the default data acquisition frequency of HailCam, to enable direct temporal and quantitative
204 comparison of observational data.

205 A particularly valuable validation opportunity arose during a rare nocturnal multi-pulse hail event on 9 May 2025 at
206 approximately 22:00-24:00 Beijing Time (UTC+8). This event featured two distinct hail pulses with maximum hailstone
207 diameters of 5–20 mm, falling over a cumulative duration of 16 minutes under low-light conditions, representing a challenging
208 scenario for optical detection systems. The disdrometer recorded continuous particle size distributions throughout the event,
209 enabling direct comparison with HailCam's imaging-based measurements. The intercomparison focused on three quantitative
210 metrics, including temporal correlation of hailfall detection and intensity variations, consistency of particle number
211 concentrations (particles $\text{m}^{-2} \text{min}^{-1}$), and agreement of hailstone size distributions. To ensure a consistent comparison with
212 HailCam which mechanically filters particles < 5 mm via its collection grid, we specifically selected disdrometer data for
213 particles with an equivalent diameter ≥ 5 mm for all statistical analyses. This intercomparison with the disdrometer's
214 established optical disdrometry capabilities provides a robust framework for assessing the accuracy and reliability of the novel
215 imaging system under operational field conditions. The detailed intercomparison results are presented in Section 3.2.

216 **3. Results and Discussions**

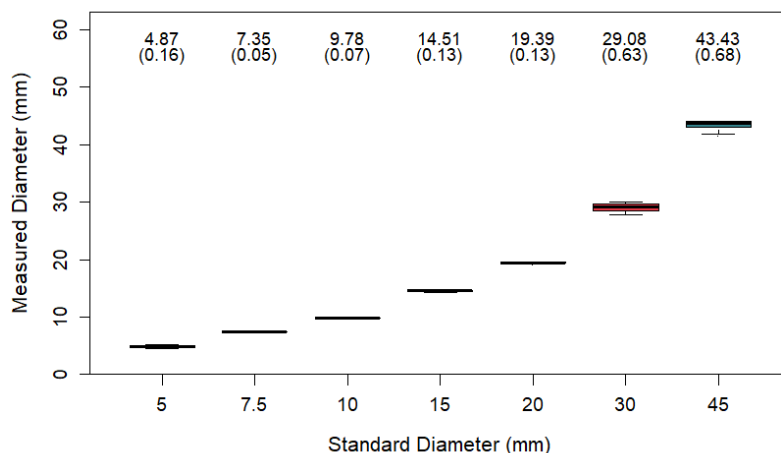
217 **3.1 Laboratory Evaluation**

218 **3.1.1 Ice Sphere Sizing Accuracy**

219 To quantitatively assess the sizing fidelity of HailCam, we performed controlled calibration experiments using synthetic ice
220 spheres across seven nominal diameter classes (5, 7.5, 10, 15, 20, 35, and 45 mm). For each size class, 50 ice spheres were
221 individually introduced onto the collection tray, and their projected silhouettes were captured and processed by the automated



222 imaging pipeline.



223

224 **Figure 4: Boxplot of measured hailstone diameters from HailCam versus seven standard reference sizes (5–45 mm). For each size**
 225 **class, 500 artificial ice spheres were individually introduced into the collection tray and automatically sized by the imaging system.**
 226 **The mean measured diameter and standard deviation (in parentheses) are labeled above each box.**

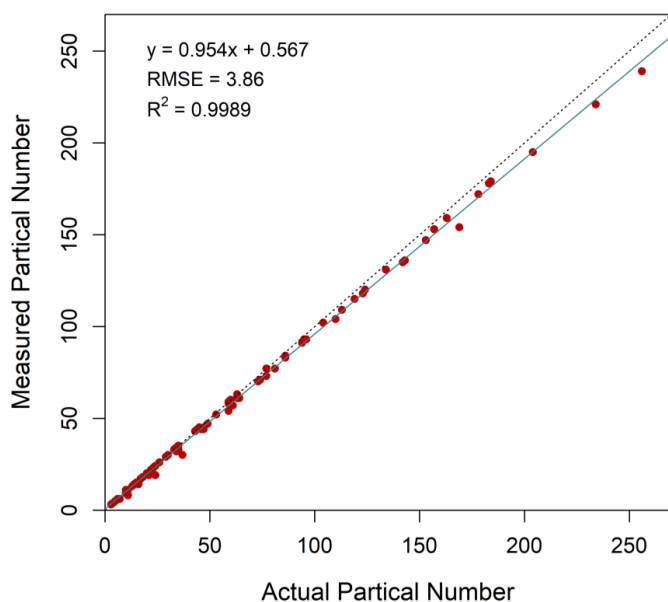
227 Figure 4 presents boxplots of the measured diameters versus the reference sizes. The system exhibits high repeatability but a
 228 systematic negative bias: the mean measured diameters are consistently smaller than the true values, with relative errors
 229 ranging from approximately 1.97% at 7.5 mm to 3.63% at 15 mm. This underestimation arises primarily from incomplete
 230 particle contour detection, where inter-particle occlusion leads to partial loss of edge information. Additionally, the standard
 231 deviation associated with each size class captures not merely random measurement noise but also spatial heterogeneity of
 232 measurement performance across the collection area. Particles landing away from the optical center experience subtle
 233 variations in lighting and viewing angle, contributing to the observed spread in measured diameters even for identical referen
 234 ce
 spheres.

235 **Table 1: The statistic metrics for evaluating hailstone diameter mean.**

Standard Diameter (mm)	5	7.5	10	15	20	30	45
Accuracy (relative error $\leq 5\%$)	72%	100%	100%	92%	98%	88%	84%
RMSE (mm)	0.21	0.15	0.23	0.57	0.62	0.95	1.71
MB (mm)	-0.13	-0.15	-0.22	-0.54	-0.61	-0.81	-1.57
NMB	-2.68%	-1.97%	-2.21%	-3.63%	-3.03%	-2.70%	-3.48%

236 Despite these effects, the overall accuracy remains sufficient for microphysical classification: 91% of measurements for
 237 particles fall within $\pm 5\%$ of the true diameter. The root-mean-square error (RMSE) increases monotonically with particle size,
 238 from 0.21 mm (5 mm class) to 1.71 mm (45 mm class), consistent with the fixed-pixel resolution of the imaging system (1.55
 239 μm pixel size, 8-megapixel sensor). This level of precision supports reliable estimation of derived quantities such as hail kinetic
 240 energy (which scales with D^3) and number concentration, both critical for severe storm nowcasting and radar algorithm
 241 validation.

242 **3.1.2 Foam Sphere Counting Accuracy**



243

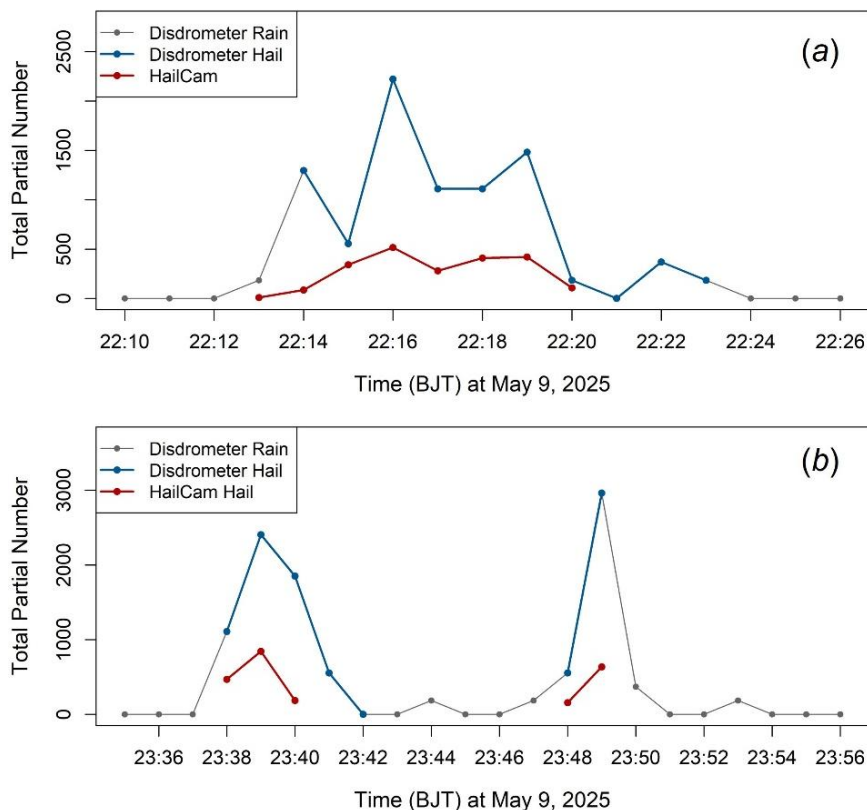
244

245 **Figure 5: Scatter plot of measured versus actual hailstone counts from 94 controlled calibration experiments.**

246 To evaluate the quantification accuracy of HailCam across varying particle number densities, we conducted 96 independent
247 trials using expanded polystyrene foam spheres of mixed diameters (5–20 mm). Each trial involved manual placement of 3 to
248 250 spheres on the collection tray in randomized spatial configurations, spanning the operational range from sparse
249 distributions (representative of marginal hailfall) to dense accumulations (approaching high-intensity hailstorm conditions).
250 Figure 5 displays the scatterplot of measured versus actual particle counts. The results reveal a strong linear relationship ($R^2 =$
251 0.9989), indicating that over 99.8% of the variance in measured counts is explained by the true values. The fitted regression
252 line $y = 0.954x + 0.567$ exhibits a slope close to unity (0.954) and a small positive intercept (0.567), confirming near-
253 proportional response across the full measurement range. The RMSE of 3.86 particles corresponds to a relative error of 4.0%
254 for counts >100 and 2.8% for small groups (<100 particles). Minor undercounting, particularly evident at higher densities
255 (>150 particles), is attributed to the reason that in dense clusters, overlapping particles can obscure edges, leading to merged
256 contours or incomplete segmentation by the ConvNeXt algorithm. Notably, the absence of significant outliers or non-linear
257 trends suggests robust algorithmic performance across variations in particle spatial distribution.



258 **3.2 Field Evaluation**



259

260 **Figure 6: Temporal evolution of total particle number with diameters ≥ 5 mm are considered, detected by the OTT Parsivel²**
 261 **disdrometer and HailCam during two hail episodes on 9 May 2025. (a) First hail episode (22:13–22:20 BJT) and (b) second hail**
 262 **episode (23:38–23:49 BJT). The disdrometer data are disaggregated into rain (grey) and hail (blue) components based on the**
 263 **instrument's classification algorithm, while HailCam measurements (red) represent hail particles with equivalent diameters ≥ 5 mm.**
 264 **Note the different scales on the y-axes between panels (a) and (b).**

265 On 9 May 2025, the HailCam system recorded two distinct hailfall episodes during a nocturnal convective event at the Weining
 266 site, revealing pronounced intra-storm variability in intensity, duration, and microphysical structure. The first episode initiated
 267 at approximately 22:14 BJT and persisted for ~12 minutes, exhibiting a multi-peaked structure with maximum particle counts
 268 reaching 2,200 min⁻¹ recorded by the disdrometer and 516 m⁻² min⁻¹ by HailCam at 22:16 BJT (Figure 6a). The second episode,
 269 including two pulses occurring from 23:38 to 23:40 BJT and from 23:48 to 23:49 BJT, displayed even higher peak intensities,
 270 with the disdrometer detecting >2,800 particles min⁻¹ and HailCam measuring 844 m⁻² min⁻¹ at 23:39 BJT (Figure 6b).

271 Comparison of the two instruments reveals both consistencies and notable discrepancies. Temporally, both systems capture the
 272 onset, peak, and cessation of hailfall with good agreement, confirming HailCam's capability to resolve the fine-scale evolution
 273 of hail events. However, substantial differences in absolute particle counts are evident: the disdrometer consistently reports 3–
 274 5 times higher total particle numbers than HailCam throughout both episodes. This discrepancy arises from fundamental
 275 differences in measurement principles and sampling geometries. The disdrometer's horizontal laser beam (30 mm wide, 180



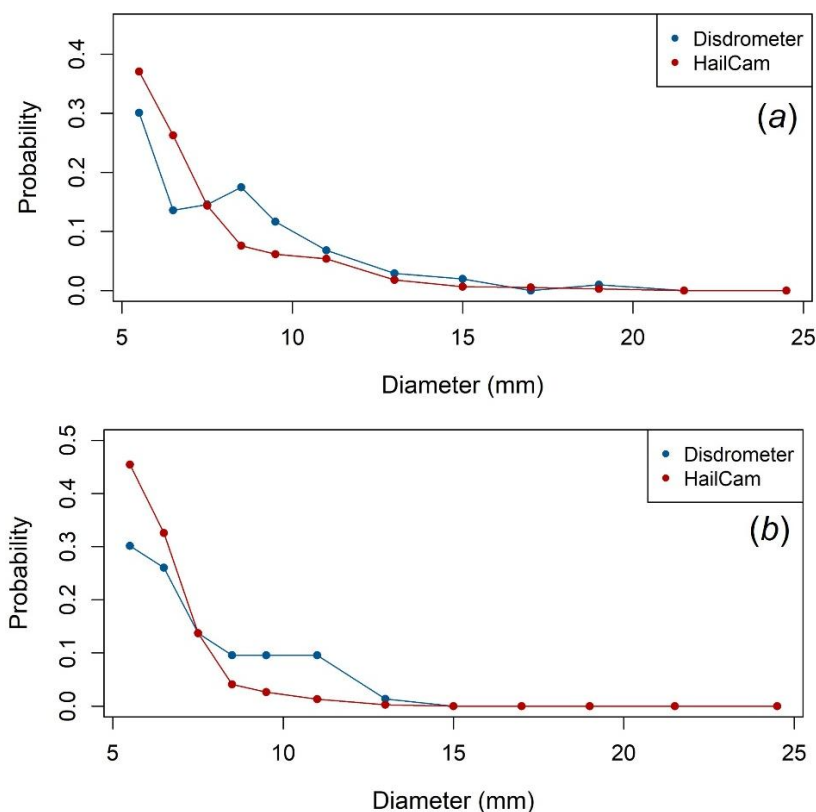
276 mm long) captures all hydrometeors passing through the sampling volume, including small ice fragments, graupel, and
277 raindrops. In contrast, HailCam's imaging-based approach applies stricter criteria (solid-phase classification via deep learning,
278 minimum 5 mm diameter threshold, and morphological validation), thereby excluding smaller or partially melted particles and
279 large rain drops that may be counted by the disdrometer.



280

281 **Figure 7: Sample image of the three hail episodes captured at Weining station.**

282 The image captured by HailCam at three time points are shown in Figure 7. The observed concentration of hail in the lower
283 left quadrant (Figure 7) is attributed to aerodynamic drag and prevailing wind direction within the collection funnel during the
284 measurement. This spatial bias reduces the effective sampling area compared to a uniform distribution. According to the
285 laboratory tests for counting accuracy in Section 3.1.2, we estimate this could introduce a systematic uncertainty of up to 5% in
286 the calculated concentration density due to edge effects and potential particle overlap in the compressed area. Furthermore, the
287 disdrometer's "hail" classification (blue dots in Figure 6) relies on empirical fall velocity thresholds, which can misidentify
288 large raindrops or conical graupel as hail, particularly during periods of mixed-phase precipitation. This is evident in Figure
289 6a during the interval 22:20–22:24 BJT, where the disdrometer continues to register substantial "hail" counts while HailCam
290 detects minimal solid precipitation, suggesting possible misclassification of heavy rain or melting particles. Conversely,
291 HailCam's negative bias may partially result from reasons that the 60-second imaging duty cycle potentially missing brief,
292 intense sub-minute fluctuations. Besides, particle overlap on the collection tray during peak intensities causing under-
293 segmentation also lead to negative observation bias.



294

295 **Figure 8: Probability density functions of hailstone equivalent diameters measured by HailCam (red circles) and the OTT**
 296 **Parsivel[®] disdrometer (blue circles) for the two hail episodes on 9 May 2025. (a) First episode (22:13–22:20 BJT) and (b) second**
 297 **episode (23:38–23:49 BJT). Diameter bins are 1 mm wide, and probabilities are normalized by the total number of particles ≥ 5**
 298 **mm detected by each instrument during the respective time periods.**

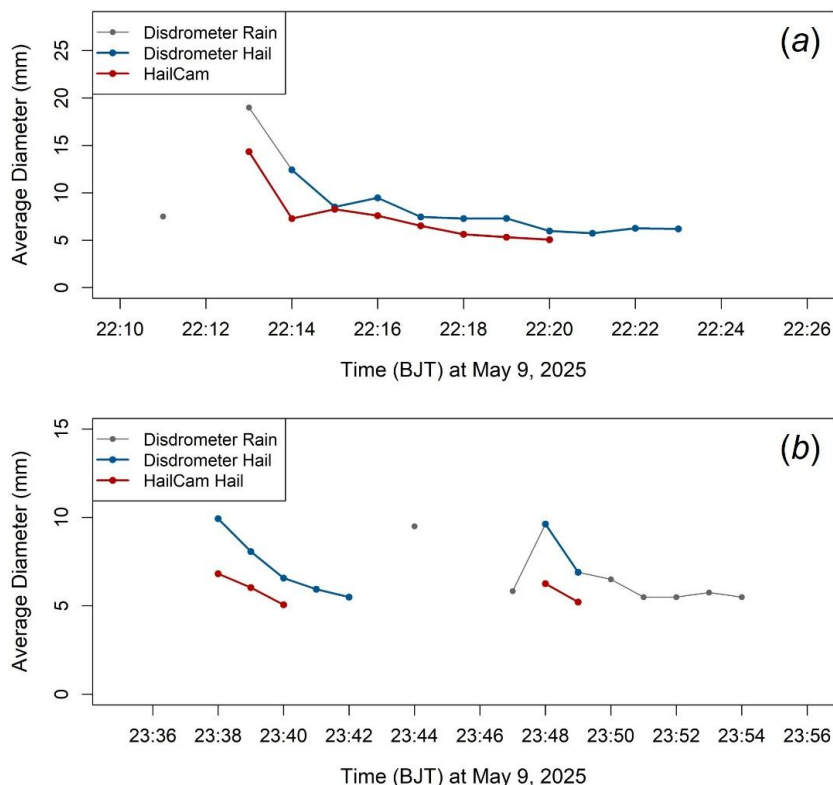
299 The hailstone size distributions (HSDs) derived from HailCam and disdrometer observations exhibit distinct patterns that
 300 reflect fundamental differences in measurement principles (Figure 8). For the first episode (Figure 8a), HailCam records a
 301 sharp dominant peak at 5–6 mm with probability 0.36, followed by a rapid monotonic decrease toward larger sizes. In contrast,
 302 the disdrometer distribution is bimodal, with a primary peak at 5–6 mm (probability 0.30) and a pronounced secondary peak
 303 at 8–9 mm (probability 0.17). Notably, the disdrometer detects substantially higher probabilities in the 7–11 mm range, while
 304 HailCam shows enhanced probabilities only at the smallest bin (5–6 mm).

305 The second episode (Figure 8b) displays even more pronounced divergence between the two instruments. HailCam again
 306 exhibits a unimodal distribution peaked sharply at 5–6 mm (probability 0.45), with near-zero probabilities beyond 12 mm. The
 307 disdrometer, however, shows a much flatter distribution with a primary peak at 5–6 mm (probability 0.30), a secondary peak
 308 at 7–8 mm (probability 0.26), and sustained probabilities of ~ 0.10 across the 8–12 mm range. This discrepancy suggests that
 309 the disdrometer's velocity-based classification algorithm may be misidentifying larger raindrops or graupel particles as hail,
 310 whereas HailCam's imaging-based segmentation strictly enforces morphological criteria for solid-phase identification.

311 Quantitative comparison reveals no statistically significant differences between the two instruments at conventional confidence
 312 levels. Kolmogorov-Smirnov tests yield $D = 0.167$ ($p = 0.996$) for the first episode and $D = 0.250$ ($p = 0.848$) for the second



313 episode, indicating failure to reject the null hypothesis of identical distributions. Despite the visual divergence in distribution
 314 shapes, particularly the disdrometer's enhanced probabilities in the 7–12 mm range, the cumulative distribution functions are
 315 sufficiently similar that the observed differences may plausibly arise from sampling variability rather than systematic
 316 measurement bias. This statistical indistinguishability suggests that both instruments capture the same underlying hail
 317 population, albeit with different detection efficiencies across the size spectrum. The disdrometer's broader tails likely reflect
 318 inclusion of marginal ice-phase particles that satisfy its velocity-based criteria, while HailCam's sharper concentration at small
 319 sizes indicates more stringent morphological filtering.
 320 These findings have important implications for operational applications. The agreement in cumulative distributions validates
 321 HailCam as a reliable alternative to established disdrometry for hail characterization, particularly given its superior phase
 322 discrimination capabilities. While the disdrometer provides continuous high-temporal-resolution measurements, its velocity-
 323 based classification may introduce uncertainty in phase identification that HailCam's imaging approach mitigates through
 324 direct morphological validation. The complementary strengths of the two instruments, disdrometer sensitivity to the full
 325 hydrometeor population and HailCam specificity for unambiguous solid hailstones, should be considered when selecting
 326 measurement strategies for radar validation or model assimilation studies.



327
 328 **Figure 9: Temporal evolution of average particle diameter measured by HailCam (red) and the OTT Parsivel³ disdrometer during**
 329 **two hail episodes on 9 May 2025. Particles with diameters ≥ 5 mm are considered. (a) First episode (22:13–22:20 BJT) and (b) second**
 330 **episode (23:38–23:49 BJT). Disdrometer measurements are separated into rain (grey circles) and hail (blue diamonds), while**
 331 **HailCam provides hail-only estimates (red circles with solid line). The time axis represents Beijing Time (BJT).**



332 The temporal evolution of average particle diameter recorded by both instruments shows broadly consistent behavior across
333 the two hail episodes (Figure 9). In both cases, the average hail diameter measured by HailCam decreases progressively as
334 each episode unfolds, from 14.2 mm at 22:13 BJT to 5.1 mm at 22:20 BJT in the first episode, and from 6.8 mm at 23:38 BJT
335 to 5.1 mm at 23:40 BJT for the first pulse and from 6.3 mm to 5.2 mm for the second pulse in the second episode. This pattern
336 suggests a shift toward smaller hydrometeors, either through the preferential melting of larger hailstones during descent or the
337 increasing dominance of smaller particles toward the end of the storm, consistent with the "size sorting" phenomenon observed
338 in previous hail studies (Knight and Charles, 2010).

339 Despite this overall temporal coherence, notable quantitative differences emerge between the two instruments. During the early
340 phase of the first episode (Figure 9a), HailCam reports substantially larger average diameters (14.2 mm at 22:13 BJT)
341 compared to the disdrometer hail classification (12.3 mm at 22:14 BJT). This discrepancy likely stems from the disdrometer's
342 velocity-based classification algorithm, which may misidentify large, irregularly shaped hailstones as raindrops or graupel due
343 to anomalous fall velocities, whereas HailCam's imaging-based approach directly measures geometric dimensions regardless
344 of particle density or shape. The disdrometer also identifies sporadic large raindrops (>15 mm) at 22:12 BJT, a signal absent
345 in the HailCam record, further highlighting the instrument's focus on solid hydrometeors.

346 In contrast, the second episode (Figure 9b) exhibits closer quantitative alignment during the main hail phase (23:38–23:42
347 BJT), with both instruments capturing a decline from ~10 mm to ~5 mm. However, HailCam misses the brief hail pulse around
348 23:48 BJT detected by the disdrometer, likely due to the 60-second imaging duty cycle or particle overlap effects during this
349 secondary intensity peak. This improved correspondence in the first half of the episode suggests that under more clearly defined
350 hail conditions, with less contamination from heavy rain or mixed-phase particles, the two measurement approaches converge,
351 reinforcing the reliability of HailCam for real-time hail monitoring when validated against established ground-based sensors.
352 Collectively, these observations demonstrate that HailCam not only provides accurate quantification of hailfall intensity but
353 also captures the temporal evolution of particle size distributions—features essential for validating radar-based hail algorithms
354 and improving convective-scale numerical models in complex terrain.

355 **3.3 Uncertainty and Error Analysis**

356 The hail observation system based on deep learning-driven image analysis demonstrates robust performance under field
357 conditions; however, several interrelated sources of uncertainty must be carefully considered when interpreting the retrieved
358 microphysical parameters. First, instrumental setup plays a critical role in measurement fidelity. Any deviation from perfect
359 orthogonality between the collection surface and the imaging plane, such as platform tilt, camera misalignment, or incomplete
360 field-of-view coverage, introduces geometric projection errors that systematically bias diameter estimates toward smaller
361 values (detailed in the Text S2 in the supplementary material). This effect is particularly pronounced for particles near the
362 edges of the imaging area, where perspective distortion is maximized. Consequently, rigorous installation protocols, including
363 precise leveling of the collection tray, calibration of focal distance, and verification of uniform illumination across the entire
364 active area, are essential to minimize spatially dependent biases and ensure consistent sizing accuracy.

365 Second, algorithmic limitations inherent to the deep learning framework contribute non-negligible uncertainty. While the
366 model achieves high detection recall under ideal conditions, it occasionally fails to identify hailstones that are small (<5 mm).
367 Based on our validation against manual counts, the algorithm exhibits an average undercounting rate of 6.8%. This
368 undercounting is primarily caused by the merging of adjacent or overlapping hailstones during image segmentation. Such
369 missed detections lead to undercounting, which propagates into biases in derived quantities such as number concentration,
370 cumulative flux, and mean particle size. Furthermore, the retrieval algorithm assumes spherical particle geometry to simplify
371 volume and kinetic energy estimation, a reasonable approximation for small hail but increasingly inaccurate for larger,



372 irregularly shaped stones commonly observed in severe storms. This shape simplification introduces systematic
373 underestimation of true cross-sectional area and mass with assumed density, especially for fractured or conical hailstones.
374 Third, real-world environmental dynamics introduce additional layers of uncertainty. During periods of intense hailfall, rapid
375 accumulation can cause some particles to be mechanically displaced into the collection bin before imaging, decoupling optical
376 counts from gravimetric measurements. Conversely, during relative warm hail-season, partial melting during the brief interval
377 between impact and image capture reduces both apparent diameter and number, skewing size distributions toward smaller bins.
378 Moreover, impacts from large hailstones can induce transient vibrations in the instrument housing, resulting in motion blur or
379 frame jitter that degrades edge sharpness and compromises contour-based sizing.
380 Collectively, these instrumental, algorithmic, and environmental factors define the current error characteristics of the system.
381 Ongoing efforts focus on integrating multi-angle imaging, implementing real-time melt-correction models, and embedding
382 physical constraints into neural network architectures to enhance robustness and reduce systematic biases in operational hail
383 microphysical retrievals.

384 **4. Conclusion**

385 In this study, we have presented HailCam, a deep learning-embedded hail observation instrument designed to address critical
386 gaps in time-resolved, ground-based hail microphysics measurements. Through integrated high-definition imaging, automated
387 sample collection, and edge-computing inference, the system delivers one-minute resolution data on hailstone number
388 concentration, and size distributions, which are essential for validating radar-based hail algorithms and constraining numerical
389 weather prediction models.

390 Multi-stage validation establishes key performance characteristics. Laboratory experiments demonstrate sizing accuracy of 91%
391 within $\pm 5\%$ relative error across the 5–45 mm diameter range, with systematic negative bias (1.97–3.63%) attributable to
392 contour detection limitations. Counting linearity exceeds 99.8% explained variance for particle densities spanning sparse to
393 dense accumulations. Field evaluation reveals agreement with reference disdrometer measurements in temporal evolution and
394 size distribution shape, despite expected discrepancies in absolute counts due to fundamentally different phase-discrimination
395 principles. The imaging-based approach provides superior specificity for unambiguous solid-phase identification compared to
396 velocity-based classification.

397 Several limitations warrant consideration. Geometric projection errors arise from non-orthogonal camera alignment.
398 Occasional under-detection affects small (< 5 mm). Environmental factors including pre-imaging particle displacement, partial
399 melting under marginal thermal conditions, and motion blur from large-stone impacts contribute additional uncertainty. The
400 60-second duty cycle may miss sub-minute intensity fluctuations during rapidly evolving events. Rigorous installation
401 protocols ensuring orthogonal imaging geometry and uniform illumination are essential for operational deployment.

402 The HailCam architecture establishes a foundation for scalable, high-fidelity hail monitoring networks. Deployment in radar
403 validation campaigns and assimilation into convective-scale ensemble systems will quantify the observational impact on severe
404 weather nowcasting. Extension to multi-sensor arrays with overlapping fields of view could enable three-dimensional hail
405 trajectory reconstruction and microphysical process studies. The dataset from the Weining experimental campaign is publicly
406 available to support community algorithm development and intercomparison initiatives.

407 **Data availability**

408 The HailCAM and disdrometer data obtained from the Weining site are accessible at Zenodo
409 (DOI 10.5281/zenodo.18585358).



410 **Author contributions**

411 BL: conceptualization, methodology, statistical and formal analysis, visualization, data curation, writing original draft, review,
412 and editing. HW: conceptualization, methodology, data curation, writing and editing. TG: conceptualization, instrument
413 deployment and maintenance, field campaign coordination. ZY: conceptualization, ground truth intercomparison design,
414 review and editing. ZZ: Conceptualization, calibration protocol development, uncertainty analysis. YD: conceptualization,
415 embedded system integration, real-time data transmission setup. YH: image preprocessing pipeline optimization, performance
416 benchmarking. XL: conceptualization, project administration, funding acquisition.

417 **Competing interests**

418 The contact author has declared that none of the authors has any competing interests.

419 **Financial support**

420 This research was funded by the National Natural Science Foundation of China Project (42475208), Experimental Research
421 on Hail Suppression Technology in Yunnan-Guizhou Plateau (ZQC-24447), Artificial Weather Modification Field Experiment,
422 Technical Research, and Benefit Assessment Service Project of Yunnan Artificial Weather Modification Centre (ZDGL-
423 W2024-004).

424 **References**

- 425 Allen, J. T., Giammanco, I. M., Kumjian, M. R., Jurgen Punge, H., Zhang, Q., Groenemeijer, P., Kunz, M., and Ortega,
426 K. L.: Understanding Hail in the Earth System, *Reviews of Geophysics*, 58, 2020.
- 427 Barras, H., Hering, A., Martynov, A., Noti, P.-A., Germann, U., and Martius, O.: Experiences with >50,000 Crowdsourced
428 Hail Reports in Switzerland, *Bulletin of the American Meteorological Society*, 100, 1429-1440,
429 <https://doi.org/10.1175/BAMS-D-18-0090.1>, 2019.
- 430 Bhandari, S., Vajpayee, G., da Silva, L. L., Hinterstein, M., Franchin, G., and Colombo, P.: A review on additive
431 manufacturing of piezoelectric ceramics: From feedstock development to properties of sintered parts, *Materials Science and*
432 *Engineering: R: Reports*, 162, 100877, <https://doi.org/10.1016/j.mser.2024.100877>, 2025.
- 433 Changnon, S. A.: Hailstreaks, *Journal of Atmospheric Sciences*, 27, 109-125, [https://doi.org/10.1175/1520-0469\(1970\)027<0109:H>2.0.CO;2](https://doi.org/10.1175/1520-0469(1970)027<0109:H>2.0.CO;2), 1970.
- 435 Cheng, L. and English, M.: A Relationship Between Hailstone Concentration and Size, *Journal of the Atmospheric*
436 *Sciences*, 40, 204-213, 1983.
- 437 Dessens, J., Berthet, C., and Sanchez, J. L.: A point hailfall classification based on hailpad measurements, *Atmospheric*
438 *Research*, 83, 132-139, 2007.
- 439 Dessens, J., Berthet, C., and Sanchez, J. L.: Change in hailstone size distributions with an increase in the melting level
440 height, *Atmospheric Research*, 158-159, 245-253, 2015.
- 441 Federer, B. and Waldvogel, A.: Hail and Raindrop Size Distributions from a Swiss Multicell Storm, *Journal of Applied*
442 *Meteorology and Climatology*, 14, 91-97, [https://doi.org/10.1175/1520-0450\(1975\)014<0091:HARSDF>2.0.CO;2](https://doi.org/10.1175/1520-0450(1975)014<0091:HARSDF>2.0.CO;2), 1975.
- 443 Fonseca-Cerda, M. d. S., de Moel, H., van Ederen, D., Schmid, T., Wouters, L., Aerts, J. C. J. H., Botzen, W. J. W., and
444 Haer, T.: Hailstorm prediction and loss assessment using high-resolution hazard and claims data, *Atmospheric Research*, 329,
445 108501, <https://doi.org/10.1016/j.atmosres.2025.108501>, 2026.
- 446 Knight and Charles, A.: On the Mechanism of Spongy Hailstone Growth, *Journal of the Atmospheric sciences*, 25, 440-444,



- 447 2010.
- 448 Kopp, J., Manzato, A., Hering, A., Germann, U., and Martius, O.: How observations from automatic hail sensors in
449 Switzerland shed light on local hailfall duration and compare with hailpad measurements, *Atmospheric Measurement*
450 *Techniques*, 16, 3487-3503, 10.5194/amt-16-3487-2023, 2023a.
- 451 Kopp, J., Schröder, K., Schwierz, C., Hering, A., Germann, U., and Martius, O.: The summer 2021 Switzerland hailstorms:
452 weather situation, major impacts and unique -observational data, *Weather*, 78, 184-191, <https://doi.org/10.1002/wea.4306>,
453 2023b.
- 454 Li, Y., Mou, X., Kang, J., Zhu, S., Fan, Y., Fan, H., Wei, X., Chen, D., Ren, S., Jia, S., Li, J., Li, N., Ran, L., Zhou, K.,
455 and Zhang, J.: The Development of a Hailstone Disdrometer and Its Preliminary Observation in Aksu, Xinjiang,
456 10.3390/atmos15070823, 2024.
- 457 List, R., Cantin, J. G., and Ferland, M. G.: Structural Properties of Two Hailstone Samples, *Journal of the Atmospheric*
458 *Sciences*, 27, 1080-1090, 2010a.
- 459 List, R., Rentsch, U. W., Byram, A. C., and Lozowski, E. P.: On the Aerodynamics of Spheroidal Hailstone Models,
460 *Journal of the Atmospheric Sciences*, 30, 653-661, 2010b.
- 461 Liu, Z., Mao, H., Wu, C. Y., Feichtenhofer, C., Darrell, T., and Xie, S.: A ConvNet for the 2020s, 2022 IEEE/CVF
462 Conference on Computer Vision and Pattern Recognition (CVPR), 18-24 June 2022, 11966-11976,
463 10.1109/CVPR52688.2022.01167,
- 464 Löffler-Mang, M. and Joss, J.: An Optical Disdrometer for Measuring Size and Velocity of Hydrometeors, *Journal of*
465 *Atmospheric & Oceanic Technology*, 17, 130-139, 2000.
- 466 Löffler-Mang, M., Schön, D., and Landry, M.: Characteristics of a new automatic hail recorder, *Atmospheric Research*,
467 100, 439-446, <https://doi.org/10.1016/j.atmosres.2010.10.026>, 2011.
- 468 Martius, O., Hering, A., Kunz, M., Manzato, A., Mohr, S., Nisi, L., and Trefalt, S.: Challenges and Recent Advances in
469 Hail Research, *Bulletin of the American Meteorological Society*, 99, ES51-ES54, <https://doi.org/10.1175/BAMS-D-17-0207.1>,
470 2018.
- 471 Mroz, K., Battaglia, A., Lang, T. J., Cecil, D. J., Tanelli, S., and Tridon, F.: Hail-Detection Algorithm for the GPM Core
472 Observatory Satellite Sensors, *Journal of Applied Meteorology & Climatology*, JAMC-D-16-0368.0361, 2017.
- 473 Nisi, L., Hering, A., Germann, U., and Martius, O.: A 15-year hail streak climatology for the Alpine region, *Quarterly*
474 *Journal of the Royal Meteorological Society*, 144, 1429-1449, <https://doi.org/10.1002/qj.3286>, 2018.
- 475 Pflaum, J. C.: New Clues for Decoding Hailstone Structure, *Bulletin of the American Meteorological Society*, 65, 1984.
- 476 Pilorz, W., Zięba, M., Szturc, J., and Łupikasza, E.: Large hail detection using radar-based VIL calibrated with isotherms
477 from the ERA5 reanalysis, *Atmospheric Research*, 274, 106185, <https://doi.org/10.1016/j.atmosres.2022.106185>, 2022.
- 478 Punge, H. J. and Kunz, M.: Hail observations and hailstorm characteristics in Europe: A review, *Atmospheric Research*,
479 176-177, 159-184, <https://doi.org/10.1016/j.atmosres.2016.02.012>, 2016.
- 480 Raupach, T. H., Martius, O., Allen, J. T., Kunz, M., Lasher-Trapp, S., Mohr, S., Rasmussen, K. L., Trapp, R. J., and Zhang,
481 Q.: The effects of climate change on hailstorms, *Nature Reviews Earth & Environment*, 2, 213 - 226, 2021.
- 482 Ravinder, A., Reddy, P. K., and Prasad, N.: Detection of Wavelengths for Hail Identification Using Satellite Imagery of
483 Clouds, *IEEE Computer Society*, 2013.
- 484 Sánchez, J. L., Gil-Robles, B., Dessens, J., Martin, E., Lopez, L., Marcos, J. L., Berthet, C., Fernández, J. T., and García-
485 Ortega, E.: Characterization of hailstone size spectra in hailpad networks in France, Spain, and Argentina, *Atmospheric*
486 *Research*, 93, 641-654, 2009.
- 487 Skripnikova, K. and Rezacova, D.: Radar-based hail detection, *Atmospheric Research*, 144, 175-185, 2014.
- 488 Smyth, T. J., Blackman, T. M., and Illingworth, A. J.: Observations of oblate hail using dual polarization radar and
489 implications for hail-detection schemes, *Quarterly Journal of the Royal Meteorological Society*, 1999.
- 490 Soderholm, J. S., Kumjian, M. R., Mccarthy, N., Maldonado, P., and Wang, M.: Quantifying hail size distributions from
491 the sky – application of drone aerial photogrammetry, *Atmospheric Measurement Techniques*, 13, 747-754, 2020.
- 492 Tokay, A., Wolff, D. B., and Petersen, W. A.: Evaluation of the New Version of the Laser-Optical Disdrometer, *OTT*

<https://doi.org/10.5194/egusphere-2026-1127>

Preprint. Discussion started: 10 April 2026

© Author(s) 2026. CC BY 4.0 License.



493 Parsivel2, Journal of Atmospheric and Oceanic Technology, 31, 1276-1288, <https://doi.org/10.1175/JTECH-D-13-00174.1>,
494 2014.
495 Wobrock, W., Flossmann, A. I., and Farley, R. D.: Comparison of observed and modelled hailstone spectra during a severe
496 storm over the Northern Pyrenean foothills, Atmospheric Research, 67, 685-703, 2003.
497